Carbohydrate Polymers 121 (2015) 37–48

Contents lists available at ScienceDirect

Carbohydrate Polymers

journal homepage: www.elsevier.com/locate/carbpol

Mechanically stable antimicrobial chitosan–PVA–silver nanocomposite coatings deposited on titanium implants

Sandeep K. Mishra [a], J.M.F. Ferreira [b], S. Kannan [a,*]

[a] Centre for Nanoscience and Technology, Pondicherry University, Puducherry 605 014, India
[b] Department of Materials and Ceramics Engineering, University of Aveiro, CICECO, Aveiro 3810 193, Portugal

ARTICLE INFO

Article history:
Received 17 September 2014
Received in revised form 2 December 2014
Accepted 3 December 2014
Available online 31 December 2014

Keywords:
Microwave synthesis
Silver nanoparticles
Bionanocomposite coatings
Chitosan
Nanoindentation

ABSTRACT

Bionanocomposite coatings with antimicrobial activity comprising polyvinyl alcohol (PVA)-capped silver nanoparticles embedded in chitosan (CS) matrix were developed by a green soft chemistry synthesis route. Colloidal sols of PVA-capped silver nanoparticles (AgNPs) were synthesized by microwave irradiating an aqueous solution comprising silver nitrate and PVA. The bionanocomposites were prepared by adding an aqueous solution of chitosan to the synthesized PVA-capped AgNPs sols in appropriate ratios. Uniform bionanocomposite coatings with different contents of PVA-capped AgNPs were deposited onto titanium substrates by "spread casting" followed by solvent evaporation. Nanoindentation and antimicrobial activity tests performed on CS and bionanocomposites revealed that the incorporation of PVA-capped AgNPs enhanced the overall functional properties of the coatings, namely their mechanical stability and bactericidal activity against *Escherichia coli* and *Staphylococcus aureus*. The coated specimens maintained their antimicrobial activity for 8 h due to the slow sustained release of silver ions. The overall benefits for the relevant functional properties of the coatings were shown increase with increasing contents of PVA-capped AgNPs in the bionanocomposites.

1. Introduction

The continuous search for better materials often includes smart combinations of several natural and/or synthetic components of different nature to extract advantages from this composite concept. Natural and synthetic polymers, metals and metallic alloys, inorganic ceramics, glass and glass ceramics offer a number of specific properties that make them attractive for biomedical applications (Ratner, Hoffman, Schoen, & Lemons, 1996). For example, titanium (Ti) and titanium alloys are widely used as structural bone implants because of their excellent mechanical properties and non-corrosiveness (Adden et al., 2006). But the longevity of Ti-based implants is limited by their poor ossseointegration ability, a problem that is often mitigated by applying surface bioactive coatings (Liang et al., 2013). Other desired properties for implant coatings might include an antiseptic action to prevent infections. In this regard, silver-based nanoparticles (AgNPs) are seen with increasing alacrity because of their high antimicrobial activity toward a broad spectrum of bacteria such as pathogens like *Staphylococcus*, *Enterococcus*, *Pseudomonas*, *Enterobacteriaceae*, etc. (Lansdown, 2002). The emergence of multiple-drug resistant (MDR) and pan-drug-resistant (PDR) (Magiorakos et al., 2012) pathogenic bacteria has also triggered immense interest in exploring the antibacterial role of AgNPs (Lara, Ayala-Nunez, Turrent, & Padilla, 2010; Rai, Yadav, & Gade, 2009). Their long-lasting biocidal activity combined with low toxicity to human cells (Williams, Doherty, Vince, Grashoff, & Williams, 1989), the biocompatibility with fibroblasts and osteoblasts (Xing et al., 2010), are stimulating their biomedical applications (Mahmoudi & Serpooshan, 2012; Podsiadlo et al., 2005). The bactericidal activity of AgNPs is attributed to the release of Ag^+ ions from soluble complexes, and surface reactions that generate reactive oxygen species (ROS) or promote catalytic oxidation of cellular components (Kittler, Greulich, Diendorf, Koller, & Epple, 2010). The antibacterial activity of AgNPs offers an opportunity to make better grafts and metal implant coatings, replacing the role of antibiotics (Taglietti et al., 2012), and reducing medicinal costs and hospitalization time. The sustainable release of Ag^+ ions acts analogous to a therapeutic substance released from a drug delivery system at or near

* Corresponding author. Tel.: +0091 413 2654973.
E-mail addresses: para_kanna@yahoo.com, skannan.nst@pondiuni.edu.in (S. Kannan).

http://dx.doi.org/10.1016/j.carbpol.2014.12.027
0144-8617/

to the targeted site inside the body (Liu, Sonshine, Shervani, & Hurt, 2010). AgNPs-loaded metal implant coatings should comply with these stringent requirements of generating a sustainable flux of silver ions around the implant to protect against bacterial infections without any extra streaming of antibiotics. Satisfying such challenges imply the synthesis and stabilization of AgNPs, the selection of a suitable matrix and a proper incorporation method.

Conventional approaches for synthesizing AgNPs require harmful chemicals, considerable amounts of heat, and generate hazardous by-products. The non-conventional microwave irradiation enables a quick and uniform heating with less energy, a higher yield of monodispersed nanoparticles and more stable against agglomeration (Hebbalalu, Lalley, Nadagouda, & Varma, 2013; Nadagouda, Speth, & Varma, 2011). Polyhydroxylated polymers are frequently used in polyol synthesis of AgNPs because they act as a reducing and capping agents and do not originate hazardous by-products. Some polyhdroxylated polymers commonly used for this purpose include polyvinyl alcohol (PVA) (Porel, Singh, Harsha, Rao, & Radhakrishnan, 2005), polyethylene glycol (PEG) (Bo, Yang, Chen, Gao, & Xue, 2009), poly(methyl vinyl ether-*co*-maleic anhydride) (PMV/MA) (Maity et al., 2011). PVA, a water soluble biodegradable polymer, is highly compatible with biopolymers and has been utilized with natural polymers like, cellulose (Nishio, Haratani, Takahashi, & Manley, 1989), lignin (Kubo & Kadla, 2003) and chitosan (Chuang, Young, Yao, & Chiu, 1999) in polymeric blends. Miscible PVA blends with biopolymers improve material performance through the formation of intermolecular hydrogen bonding (Matsumura, Tomizawa, Toki, Nishikawa, & Toshima, 1999). Among natural polymers, CS, a cationic heteropolyaminosaccharide derivative of chitin consisting of 2-amino-2-deoxy-D-glucopyranose and *N*-acetyl-2-amino-2-deoxy-D-glucopyranose (Wan, Wu, Yu, & Wen, 2006), offers remarkable features that make it for biomedical applications. The attractive features include non-toxicity, biodegradability, biocompatibility, bioadhesive and absorption enhancing properties (Kim et al., 2008). The main CS related difficulties include poor processing ability and weak mechanical properties, which might be overcome by blending CS with other natural or synthetic polymers to obtain superior materials for the regeneration of several damaged tissues such as nerves (Jiao et al., 2009), bone cells (Malafaya & Reis, 2009), skin (Zhou et al., 2008) and cartilage (Kuo & Ku, 2008). CS has also been proposed for wound dressing and water disinfection applications due to its intrinsic antimicrobial activity. The disinfectant role of CS is attributed to amino groups (p*Ka* = 6.4–6.7) that exert an efficient antimicrobial activity under the protonated condition i.e., in acidic solution. Strategies for preserving the antibacterial activity of CS at the physiological pH, include: (i) modifications with iodinated compounds; (ii) incorporation of antibodies (Mi et al., 2002); (iii) chelation of metal ions like Ag^{+}, Cu^{2+}, Mn^{2+} or Fe^{2+} (Du, Niu, Xu, Xu, & Fan, 2009; Wang, Du, Fan, Liu, & Hu, 2005); (iv) embedding AgNPs (Mironenko, Modin, Sergeev, Voznesenskiy, & Bratskaya, 2014; Tiwari, Mishra, Mishra, Kuvarega, & Mamba, 2013).

Ideally, implant coatings should be antibacterial, cytocompatible, and mechanically stable. Although some literature reports about CS-based biocompatible coatings on Ti substrates are available (Lina & Chen, 2013), no systematic studies of mechanically stable bionanocomposite of CS have been reported so far. The present work aims at synthesizing PVA-capped AgNPs by a microwave assisted route, investigating their potential as nanofiller for improving the mechanical properties of CS matrix, and evaluating the long term antibacterial activity of the multifunctional bionanocomposites coatings deposited onto Ti substrates toward gram positive and gram negative bacteria.

2. Materials and methods

2.1. Materials and reagents

Commercially titanium (Ti) (Ti—99.67, C—0.08, Fe—0.03, N—0.03, O—0.18 and H—0.015) was selected as substrate. PVA (MW = 140 kDa), acetic acid, glutaraldehyde solution (25%), (3-amino propyl) triethoxysilane (APTES) and ammonia solution were purchased from Hi-media, India. High purity chitosan (CS) with medium molecular weight (Sigma-Aldrich, deacetylation ~80%) was further purified by dissolving 1 g of CS in 100 mL of 5% w/v acetic acid solution for 24 h and filtering through a series of Nylon-66 hydrophilic syringe membranes (Hi-media, India, pore sizes: 1, 0.45, and 0.22 μm). CS was then precipitated by adding 25% ammonia solution and separated by centrifugation at 6000 rpm for 10 min at 4 °C. This purified chitosan was washed thrice with doubly deionized water and lyophilized at −80 °C for 24 h. Silver nitrate (Sigma-Aldrich, 99.98% purity) was selected to synthesize the AgNPs. For antibacterial assays, trypton-glucose-yeast extract (TGY) broth and agar powder of bacteriological grade were purchased from Hi-media, India.

2.2. Method of synthesis

2.2.1. Preparation of Ti substrates

A polishing machine (BAINPOL-VTD, India) was used to smooth the surface of square (10 mm × 10 mm × 2 mm) Ti substrates by successively grinding with abrasive silicon carbide (SiC) sheets of different grit sizes: 80, 220, 400, and 1000, corresponding to about 200, 68, 35, and 18 μm, respectively, followed by a final polishing with 3 μm diamond paste. The as polished Ti substrates were cleaned by sonication for 10 min in each of the following media: acetone (70 vol.%), ethanol (70 vol.%), and deionized water. The metal samples were then passivated in a 1:5 (v/v) nitric acid-deionized water solution for 30 min at 40 °C, rinsed with deionized water for several times and placed in sealed Teflon container to avoid surface contamination.

2.2.2. Synthesis of silver nanoparticles (AgNPs)

For the synthesis of AgNPs, two aqueous stock solutions were firstly prepared: (i) 5 mg mL^{-1} of PVA in double deionized water; (ii) 20 mM $AgNO_3$ with a pH value ~12 adjusted by adding the required amount of ammonia, and kept under stirring for 30 min. Fixed aliquots of stock PVA solution were added to Erlenmeyer flasks and mixed with three different amounts of stock $AgNO_3$ solution to obtain final volumes 20 mL with a constant final concentration of PVA = 2.5 mg mL^{-1} and three different Ag concentrations of 0.01 mM, 0.1 mM and 10 mM (coded respectively as Ag—0.01, Ag—0.1 and Ag—10). The pH of all solutions was maintained at ~10 by adding the required amounts of ammonia and the flasks, tightly plugged with cotton wool, were then irradiated in a microwave oven for 90 s at a constant power of 60 W. Upon this treatment, the solution color turned from transparent to golden yellow, confirming the successful synthesis of PVA-capped AgNPs. After the completion of reaction, the solutions were immediately cooled in ice bath and the total volume was adjusted to 20 mL by adding small amounts of double deionized water to compensate for water loss due to irradiation.

2.2.3. Synthesis of CS/PVA-capped AgNPs composite systems

A stock solution (10 mg mL^{-1}) of CS in 1% acetic acid was firstly prepared. Then, aliquots of this solution were added to the PVA-capped sols of AgNPs obtained as described in Section 2.2.2. A constant CS:PVA weight ratio of 1:4 (monomeric unit ratio of CS:PVA = 1:1) was fixed for all bionanocomposite systems and the

resulting mixtures containing 5 mg mL^{-1} of CS were kept under stirring (600 rpm) for 3 h at 40 °C.

2.2.4. Deposition of antimicrobial bionanocomposite coatings

The Ti substrates prepared as described in Section 2.2.1 were soaked in an ethanol solution of APTES (5% v/v) for 1 h for surface silanization, gently rinsed in ethanol and dried at 120 °C for 2 h. The samples were then submerged in a 2% (v/v) glutaraldehyde solution overnight, rinsed with deionized water and dried at room temperature. A simple spread casting method was adopted to make a uniform coating on the Ti surface. 100 μL of the bionanocomposite solutions were homogeneously spread onto the pretreated Ti substrates (1 cm^2) and dried at room temperature in a vacuum oven for 24 h. For growth inhibition assay, Ti specimens were coated on both sides similarly as mentioned above. The dry coated Ti substrates were stabilized in 2 N NaOH for 5 min and washed in deionized water for further characterization.

2.3. Characterization techniques

UV–visible (UV–vis) absorption spectra of the bionanocomposite solutions were recorded in a UV–vis spectrophotometer (PERKIN ELMER LAMBDA 650 S) using a quartz cell of path length 1 cm. Photoluminescence (PL) spectra were gathered on a spectrofluorometer (PERKIN-ELMER LS 50B) with a xenon discharge lamp excitation. The crystalline state of AgNPs was analyzed using a high resolution X-ray diffractometer (RIGAKU, ULTIMA IV, Japan) with Cu $K\alpha$ radiation ($\lambda = 1.5406$ Å) produced at 40 kV and 30 mA to scan the diffraction angles (2θ) between 5° and 90° with a step size of 0.02° 2θ per second. For this, the PVA-capped AgNPs colloidal sols were centrifuged (EPPENDORF, Germany) at 12,000 rpm for 20 min. The sediments were re-dispersed in 70% ethanol by bath sonication and then centrifuged again. This redispersion-centrifugation process was repeated thrice to wash off the remaining residues followed by washing with double distilled water and drying the resultant powders in a vacuum oven at 50 °C for 24 h. The composite coatings were also characterized by XRD analysis.

The miscibility between CS and residual PVA was assessed through differential scanning calorimetry (DSC) and thermogravimetric analysis (TGA), performed in nitrogen atmosphere at a heating rate of 10 °C min^{-1} in a simultaneous thermal analyzer (TA INSTRUMENT Q600 SDT), using dried bionanocomposites samples. A heating–cooling–heating (H–C–H) cycle was firstly run to remove the moisture content and determine the glass transition temperature (T_g). The samples were cooled back to room temperature (RT) and finally heated up to 600 °C.

Fourier transform infrared spectroscopy (FT-IR) analysis of pure CS and PVA and of CS/PVA-capped AgNPs composite systems was performed in transmission mode using a FT-IR spectrophotometer (PERKIN–ELMER, USA) in the spectral range from 4000 to 400 cm^{-1}. The dried samples were diluted in KBr and pelletized. Raman spectra were also recorded for coated Ti substrates using a confocal Raman microscope (RENISHAW, UK) at an excitation wavelength of 785 nm.

The particle size analysis of AgNPs was carried out on a Malvern Nano S Zetasizer, with a backscattering angle of 90° and a 'He laser' of wavelength 632.8 nm using 3 mL disposable plastic cuvettes. Cuvettes were cleaned of dust using compressed air and loaded underneath a fume hood using a 0.22 μm syringe filter (Himedia) to minimize dust interference. Size measurements were computed by collecting at least 12 runs performed with counting rates varying between 400 and 600 kilo counts per second (kcps).

2.4. Surface analyses of bionanocomposite coatings

The surfaces of CS/PVA-capped AgNPs composite coatings were observed by scanning electron microscopy (SEM) with an Energy-dispersive X-ray spectrometer (EDX), operating at 10 kV acceleration voltage after being coated with a thin layer of carbon (HITACHI E1010 ion sputter). Tapping mode atomic force microscopy (AFM, BRUKER MM8, USA) was used to assess the surface roughness and topography of the coatings in 1×1 μm areas. Root mean square (RMS) roughness values were taken from 10 measurements performed on different locations over each sample. High resolution (512×512 pixel) scan was performed to and the results were analyzed using Nanoscope software (v1.30).

2.5. Mechanical properties

The mechanical properties of bionanocomposite coated Ti substrates were determined using a Nanoindenter machine (BRUKER-CETR, USA). The load-displacement behavior under hydrated and dehydrated conditions was assessed using a Berkovich indenter tip to determine elastic modulus and hardness using a conventional depth-sensing test. The measurement cycle (load/unload-displacement curves) consisted of a loading segment followed by a dwell time of 30 s at maximum load and finally an unloading segment. A total of 20 indentations were performed for across the surface of the specimens under an applied load of 300 μN. Under hydration conditions, the samples were soaked in a phosphate buffer saline (PBS) solution (pH 7.4) incubated at 37 °C for 6 h.

2.6. Silver ion release and antibacterial tests

The antibacterial activity of AgNPs is mainly due to the release of silver ion (Ag^+). The coated samples were soaked in 5 mL of PBS solution incubated at 37.2 °C and the Ag^+ concentrations released from coatings were quantitatively determined (within the range up to 0.01 ppm) after different incubation time periods (1 h, 6 h, 12 h, 24 h, 48 h, 72 h, 96 h and 120 h) by ICP-AES (ARCOS, SPECTRO, Germany).

Antibacterial tests were carried out via 'modified disc diffusion assay' and 'growth inhibition assay'. *Escherichia coli* and *Staphylococcus aureus* were chosen as Gram negative (G^-) and Gram positive (G^+) bacteria models, respectively. Cultures of both the bacteria were grown in TGY broth at 37 °C in a shaking incubator for 12–16 h. For the modified disc diffusion assay, 1.5% agar mixed TGY broth was prepared and 25 mL this was transferred into petri dish. Then, 100 μL bacterial cultures were uniformly spread onto the inoculated surfaces of bionanocomposite coatings and the samples were incubated at 37 °C overnight and inhibition zones were analyzed. For growth inhibition test, 5 mL of TGY broth was taken in test tubes and to each, a both side coated sample inoculated with 200 μL of test organism was then added. All experiments were performed in triplicate. For analyzing growth inhibition of bacteria, 200 μL of samples were collected at predetermined time intervals in 'biochemical grade 96 well plate' and optical density at 600 nm (OD_{600}) was recorded on 'ELISA reader' (VERSAMAX ELISA MICROPLATE READER). All data reported were subtracted with the OD_{600} of media without bacterial inoculum. A test tube with same amount of TGY broth and bacterial inoculum was used as a positive growth control and mentioned as 'control'. All nutrient media and glassware were sterilized in an autoclave at 121 °C and 15 psi (~103 kPa) for 20 min and UV treated before performing the experiments.

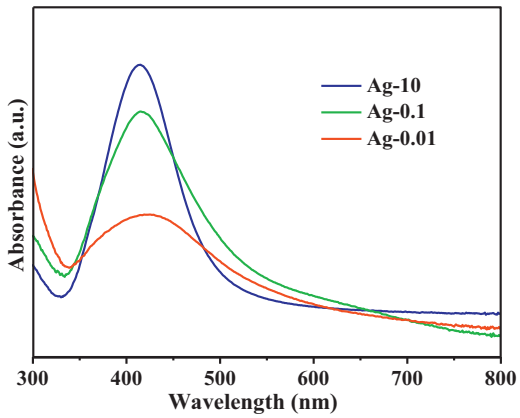

Fig. 1. UV–vis absorbance spectra of PVA-capped AgNPs. Relative λ_{max} occurred at 410 nm, 412 nm and 415 nm for Ag—10, Ag—0.1 and Ag—0.01, respectively.

3. Results and discussion

The results will be discussed taking into account the key objectives of the present work: (1) the 'green' synthesis of AgNPs; (2) the deposition of mechanically stable, biodegradable and antibacterial nanocomposites coatings on the surface of Ti implants; (3) assessing the physical, chemical, and mechanical properties of bionanocomposites coatings; (4) characterizing their long term antibacterial efficacy through the controlled release of Ag^+ ion.

3.1. UV–vis spectroscopy

The optical absorption spectra of the PVA-capped AgNPs solutions are presented in Fig. 1. Only single, relatively narrow and symmetric peaks can be observed in all the spectra, a feature that is mainly attributed to primary dipolar excitation (Hu, Wang, Wang, Zhang, & Yu, 2008). Surface plasmon resonance (SPR) absorbances are observed at 410 nm, 412 nm and 415 nm for the Ag—10, Ag—0.1 and Ag—0.01 AgNPs, respectively. These intrinsic SPR spectral features typically occurring within 380–420 nm range, depending on size and shape of AgNPs and capping agents (Kahrilas et al., 2014a,b), arise from the coupling between the conduction band electrons on the AgNPs surface with the incident electromagnetic radiation (Bohren & Huffman, 1983; Kreibig & Vollmer, 1995). The SPR band was broader for Ag—0.01 thus indicating the presence of silver nanoparticles with broader size distribution. The absorption peak became gradually sharper and with enhanced intensity for Ag—0.1 and Ag—10. The symmetry of SPR spectra demonstrates the low level of agglomeration in colloidal state (Vigneshwaran, Nachane, Balasubramanya, & Varadarajan, 2006).

3.2. Photoluminescence (PL) spectroscopy

The PL spectra of the PVA-capped AgNPs sols presented in Fig. 2 shows emission peaks that depend on the photo-excitation wavelength, being centered at 475 nm when excited at 408 nm (Gao et al., 2004), and red shifted to 504 nm upon excitation at 430 nm (Kahrilas et al., 2014a). The emission range reported in literature (465–630 nm) depends primarily on the size of AgNPs and their capping agents (Gao et al., 2004; Simo et al., 2012; Vigneshwaran et al., 2006). When excited at 490 nm, the emission red shifted to 589 nm with an additional peak occurred at 536 nm.

The red shifting trend accentuated upon further increasing the excitation wavelength to 510 nm with the main emission peak appearing at 618 nm and two smaller ones at 560 nm and 765 nm. Such trend, accompanied with a reduction in intensity of the peaks is consistent with findings reported elsewhere (Vigneshwaran et al., 2006). The analysis of emission spectra of AgNPs obtained from the four different excitation wavelengths reveals that photoemission is independent of the particle size while the intensity increases sharply from lower to higher AgNPs concentrations. This luminescence in visible range is due to the excitation of electrons from occupied *d* bands into states above the Fermi level. Subsequent electron–phonon and hole–phonon scattering processes lead to an energy loss and, finally, to photoluminescent radiative recombination of an electron from an occupied *sp* band with the hole (Smitha, Nissamudeen, Philip, & Gopchandran, 2008).

3.3. Phase analysis

The XRD patterns of the synthesized AgNPs presented in Fig. 3A shows relatively sharp peaks located at 2θ angles of 38.1°, 44.3°, 64.4°, 77.4° and 81.5°, which coincide with those of standard crystalline silver (ICDD card No. 03-065-2871). These peaks corresponding to (1 1 1), (2 0 0), (2 2 0), (3 1 1) and (2 2 2) planes of the face-centered cubic (FCC) Ag confirm the successful synthesis of crystalline AgNPs. A broad peak centered at ~20° 2θ is attributed to PVA used as capping agent during the synthesis as can be deduced from the typical XRD peak of pure PVA appearing at this 2θ angle in the magnified intensity scale of Fig. 3B. These results enable concluding about the absence of crystalline impurities in the synthesized AgNPs. The XRD patterns of composite coatings on Ti substrates are presented in Fig. 3C. The dominant Ti peaks were truncated to allow detecting the less intense signals from AgNPs and embedding polymer. A broad peak at ~20° 2θ corresponds to the polymeric CS/PVA matrix.

3.4. Thermal analysis

The differential scanning calorimetry (DSC) curves obtained for pure CS, pure PVA and all bionanocomposites (Ag—10, Ag—0.1 and Ag—0.01) are presented in Fig. 4A. A good miscibility in polymer blends is commonly translated by a single composition-dependent T_g. The CS DSC curve shows a broad endothermic peak at 75 °C and a sharp exothermic peak at 306 °C, which are, respectively, due to the elimination of moisture from the polymer matrix, and to the decomposition of saccharine structure in chitosan. For bionanocomposites, the endothermic peaks centered at 69 °C (Ag—10, Ag—0.1) and 75 °C (Ag—0.01) also account for the removal of moisture, while the broad exothermic ones at 245 °C (Ag—10), 275 °C (Ag—0.1) and 280 °C (Ag—0.01) are similarly due to thermal degradation of the polymer matrix. This is supported by the thermograms of pure CS, pure PVA and synthesized AgNPs containing bionanocomposites plotted in Fig. 4B.

Pure chitosan underwent a weight loss of 18% until 150 °C due to evaporation of adsorbed water. Similar phenomenon explains the weight losses experienced by Ag—10, Ag—0.1 and Ag—0.01 up to 150 °C. The higher moisture contents of bionanocomposites in comparison to pure CS might be attributed to the hydrophilic character of PVA. On the other hand, the comparison of the Ag—10, Ag—0.1 and Ag—0.01 thermograms shows that moisture contents tend to decrease with increasing amount of incorporated AgNPs as expected. At 600 °C there was nearly no residue left by PVA, while an ash content of 32% remained in the case of CS. The residual weight left at this temperature is more in case of bionanocomposites and increases with increasing the AgNPs contents as expected.

From the H–C–H cycle (Fig. 4C), a single T_g value at about 218 °C was estimated for Ag—0.01 and Ag—0.1, while T_g values for pure CS and PVA were recorded 230 °C and 75 °C, respectively. Table S1 (Supporting information) reports relevant data derived from DSC and TGA measurements. These results suggest that a high miscibility level between CS and PVA has been achieved in all bionanocomposites. This excellent miscibility can be understood

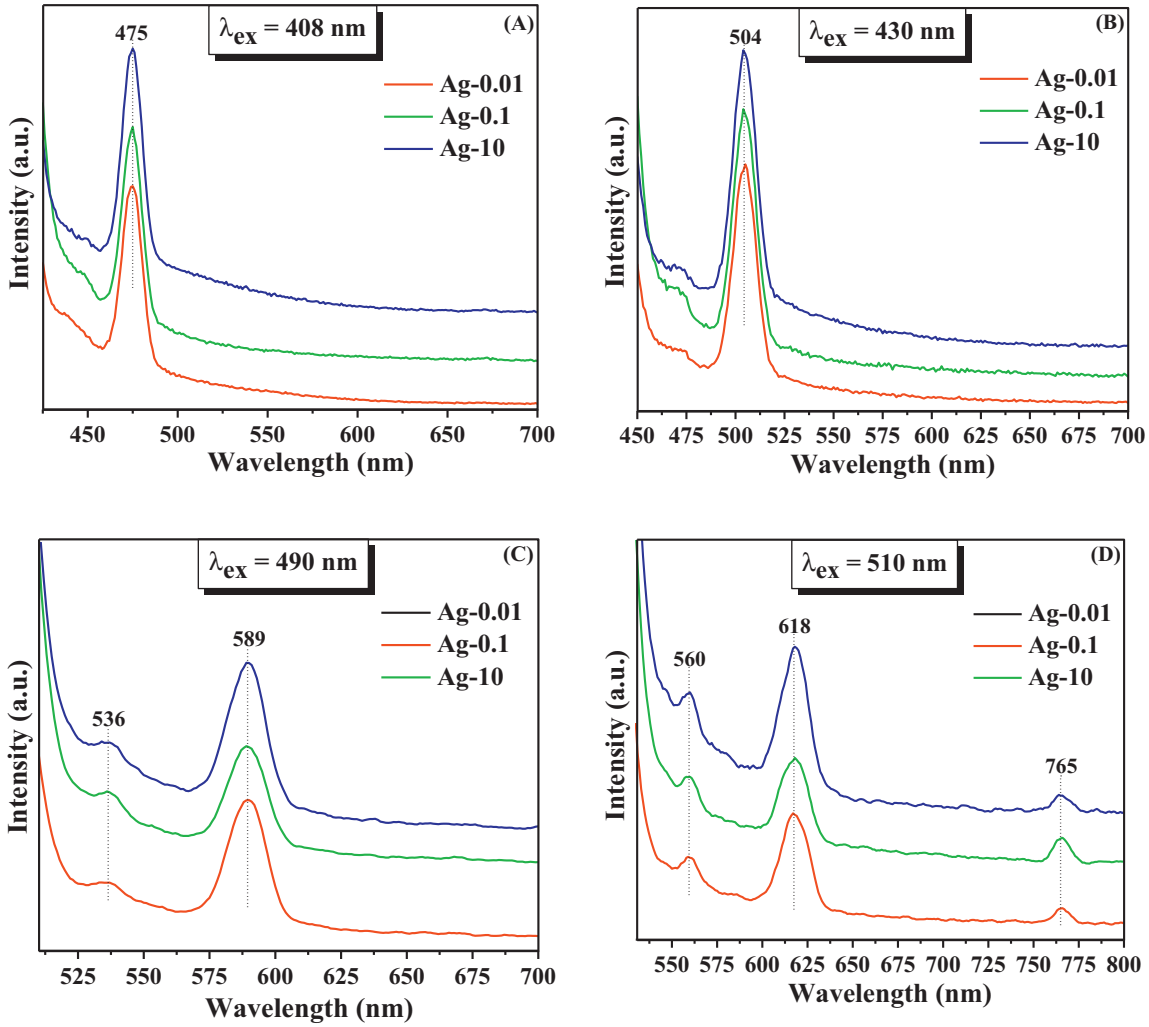

Fig. 2. Emission spectra of all synthesized PVA-capped AgNPs excited at (A) 408 nm, (B) 430 nm, (C) 490 nm and (D) 510 nm.

considering the expected mutual interaction between the abundant hydroxyl groups of PVA and amino group in CS to form strong hydrogen bonds, which tends to depress the melting point (T_m). The mixing of amorphous/crystalline polymers can result in depression in T_m and stronger the interactions between both polymers will give rise to more accentuated depression in T_m (Kubo & Kadla, 2003). The amount of PVA capping AgNPs is expected to be higher in Ag—10 in comparison to the other bionanocomposites, and should therefore lead to stronger CS-PVA interactions. This might help explaining why the determination of the T_g was complicated in the case Ag—10 owing to its earlier thermal degradation, and why its T_m is the lowest.

3.5. Fourier transform infra-red (FT-IR) and confocal Raman spectroscopy

FT-IR analysis was used to assess the chemical features of CS and PVA and intermolecular interaction in bionanocomposites. The FT-IR spectra of pure CS and PVA and of the composite samples Ag—10, Ag—0.1 and Ag—0.01 are shown in Fig. 5A. The CS peaks of CS at 890 cm^{-1} and 1155 cm^{-1} are ascribed to the presence of pyranose ring in the saccharin structure. The broad band around 3600–3000 cm^{-1} is due to the N—H and O—H stretching. The bands at 2925 and 2876 cm^{-1} are due to the C – H aliphatic stretching vibrations. The three bands appearing at 1653, 1590, and 1256 cm^{-1} are, respectively, assigned to the stretching of the carbonyl (C=O-NHR) group (amide-I), N—H stretching of the secondary amide (amide-II), and amide-III of chitosan (Angadi, Manjeshwar, & Aminabhavi, 2011). The typical PVA peaks include a large band at 3522 cm^{-1} (O—H stretching), the peaks at 2913 cm^{-1} (C—H stretching from alkyl groups), 1740 cm^{-1} (C=O stretching) and 1140 cm^{-1} (crystalline C=O stretching of semicrystalline PVA). In the Ag—10, Ag—0.1 and Ag—0.01 samples, the characteristic peaks of CS and PVA are seen with a small shift in their frequencies. The peak at 1140 cm^{-1} of PVA was significantly reduced, indicating the loss in regularity of the PVA polymer chains due to inter-polymer interaction with CS (Mansur, Costa, Mansur, & Barbosa-Stancioli, 2009). In bionanocomposites, shifts from 3420 cm^{-1} to 3447 cm^{-1}, 3512 cm^{-1} and 3490 cm^{-1} for Ag—10, Ag—0.1 and Ag—0.01, respectively, were observed with a sharp increase, indicating enhanced hydrogen bonding due to CS–PVA chain interactions.

The amide band at 1653 cm^{-1} for pure CS shifted to a lower wavenumbers: 1646 cm^{-1}, 1651 cm^{-1} and 1653 cm^{-1} for Ag—10, Ag—0.1 and Ag—0.01, respectively. These shifts clearly imply interactions between CS and PVA-caped AgNPs. The more pronounced shift in the case of Ag—10 is consistent with a higher PVA content capping the AgNPs, in good agreement with the results of thermal analysis. In addition, the bands at 1596 cm^{-1}, assigned to amide II, and at 1256 cm^{-1}, assigned to amide III, also shifted toward lower wavenumbers in all bionanocomposites. Increasing content

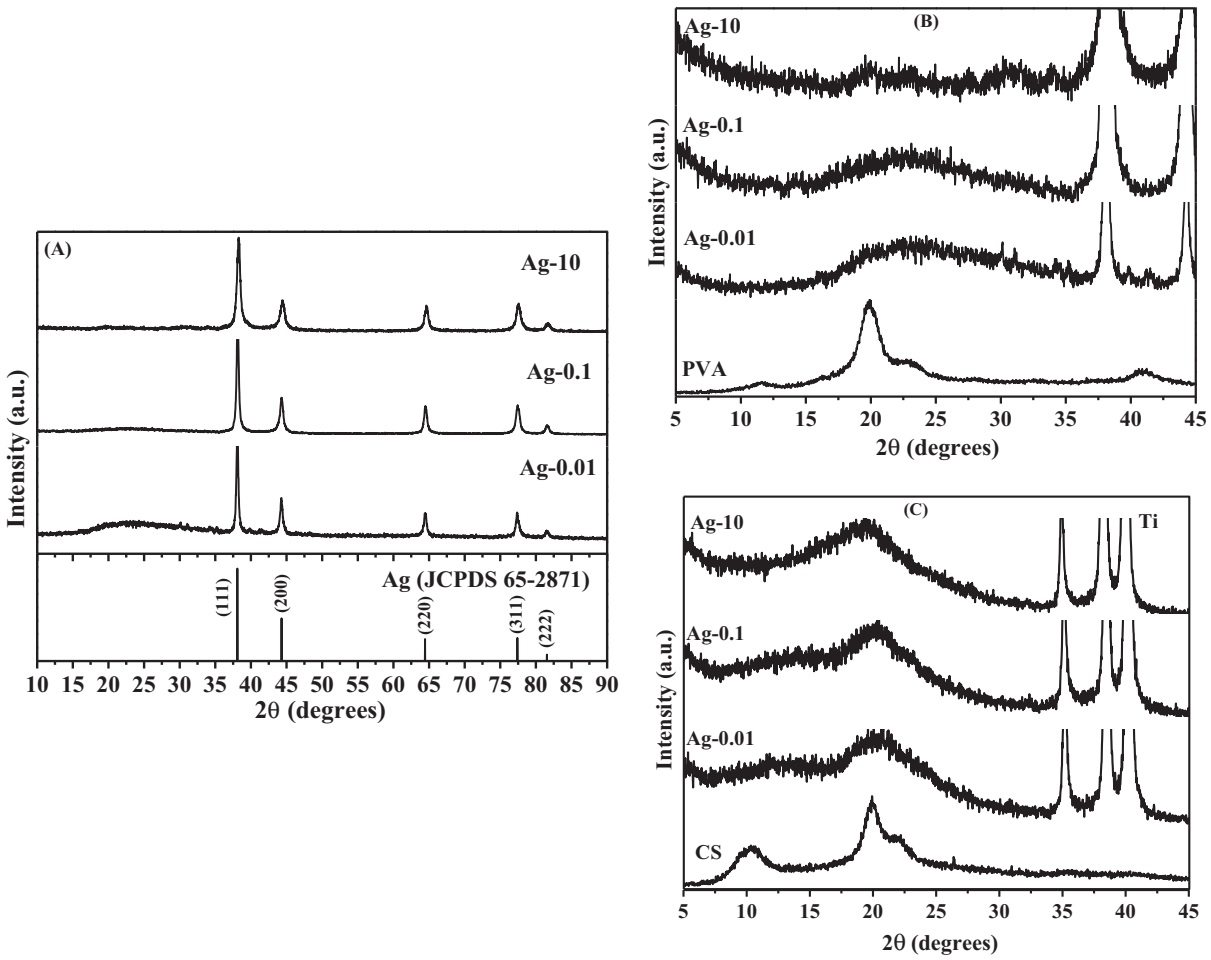

Fig. 3. Powder XRD patterns of: (A) PVA-capped AgNPs, (B) of PVA-caped AgNPs within a limited 2θ range and magnified intensity scale, and (C) bionanocomposites coatings on Ti metal.

of AgNPs (and capping PVA) resulted in sharpening and shifting of amine bands, suggesting close proximity of AgNPs to the CS. The division of combined peak of amide I and amide II at 1653 cm^{-1} and 1590 cm^{-1} also reflects the interactions between Ag, O and N atoms of these groups. These are clear evidences of the involvement of primary amino and amide groups in the interactions with the metal. The amine ($-NH_2$) groups can electrostatically interact and coordinate with Ag^+ ions adsorbed over the surface of AgNPs, avoiding agglomeration of reduced Ag^0. This ability to act as surface modifier justified the use of amine containing reagents as capping sites for AgNPs (Jin & Bai, 2002; Roldan, Scaffardi, Sanctis, & Pellegri, 2008; Wei, Sun, Qian, Ye, & Ma, 2009).

The bands at 1417 cm^{-1} (bending vibration of OH group), 1376 cm^{-1} (symmetric deformation vibration mode of CH_3), and 1320 cm^{-1} (CH_2 wagging vibration mode in primary alcohol) were not much affected for the lower concentrations of AgNPs (Ag—0.01 and Ag—0.1). However, these three peaks merged to a single band at 1388 cm^{-1} in the case of Ag—10, strongly suggesting the occurrence of interactions between AgNPs and CS via PVA-capping agent.

For the bionanocomposite coatings on Ti substrates, the interactions between CS and PVA-capped AgNPs were also assessed through Raman spectroscopy. In order to ensure the reproducibility of Raman shift, five spectra were collected from different spots of each sample. Although for a given sample the intensity of Raman peaks can vary from one spot to another due to variations in AgNPs density, the results were quite reproducible. Therefore, a typical spectrum of each sample was selected after being scaled based on the intensity of the band at 1378 cm^{-1}, due to its fairly stable relative intensity and ascribed to the vibration of chitosan backbone. The Raman spectra displayed in Fig. 5B reveal stronger peaks for non-polar vibrations than for polar ones in comparison to FT-IR.

The Raman spectrum of CS was very similar to its major monomeric constituent *D*-glucosamine obtained by She, Dinh, and Tu (1974) and by Gelder, Gussem, Vandenabeele, and Moens (2007) Raman shifts at 898 (C—H vibration of β-anomeric residues), 1086, 1262, and 1378 (C—O deformation of a secondary alcoholic group) cm^{-1} remained almost constant when the concentration of AgNPs increased from samples Ag—0.01 to Ag—10, contrasting with the dramatic increase in intensity of the bands at around 1042 cm^{-1}; moreover, a new band at around 854 cm^{-1} as a shoulder of 898 cm^{-1} band appeared. From FT-IR and Raman spectroscopy, it can be deduced that the cross-linked polymers are present as interpenetrating networks. The Raman spectrum of CS exhibited characteristic absorption bands at 3299 cm^{-1} assigned to N—H stretching and 1458 cm^{-1} assigned for C—N stretching of a primary amine were diminished as the AgNPs content increased and disappeared in Ag—10 (Lillo & Matsuhiro, 1997). This result supports the interactions between amine groups of CS and the positively polarized surface sites of AgNPs as revealed from FT-IR analysis. The intensity of Raman peak at 1040 cm^{-1} assigned to C—OH was significantly enhanced with increasing AgNPs contents in the coatings and became the prominent peak in Ag—10. This result demonstrates the increasing dipolar interactions involving OH groups with increasing AgNPs contents, an aspect that was not enough clear from FT-IR spectra. This is also supported by the broadening of 568 cm^{-1} peak assigned to the skeleton modes

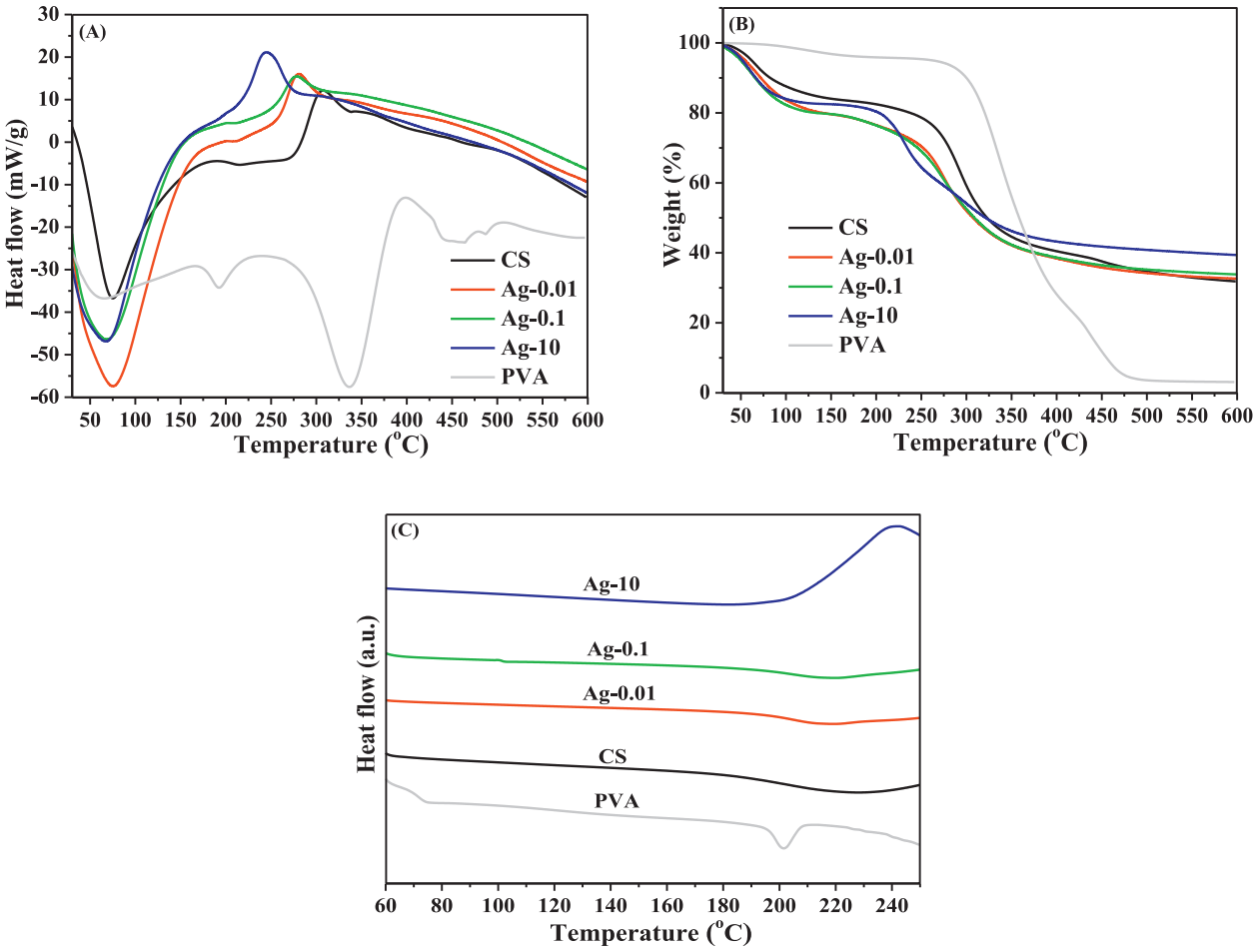

Fig. 4. Thermograms of bionanocomposites: (A) DSC, (B) TGA, (C) DSC curve of heating–cooling–heating (H–C–H) cycle.

of CS as AgNPs contents increase. The peaks at 2886 cm^{-1} and 2928 cm^{-1} can be attributed to the stretching vibration of CH and CH_2. The dipolar interaction between CS and PVA groups should have changed the vibration modes of CH and CH_2 groups, so that the peak at 2886 cm^{-1} shifted toward 2928 cm^{-1} and merged in a broad peak. There were no significant changes in the bands at 1094 and 1116 cm^{-1}, which are ascribed to symmetric vibrations of glycosidic bonds (Zhang, Peschel, Helm, Groth, & Fischer, 2011). These results demonstrate the non-covalent interactions between PVA-capped AgNPs and CS.

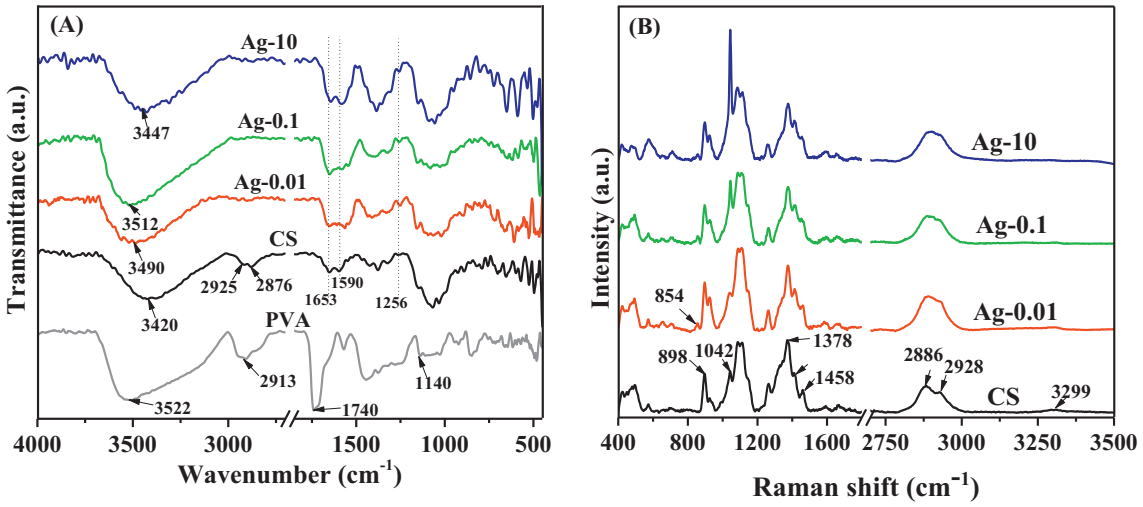

Fig. 5. FT-IR spectra of pure PVA, pure CS and bionanocomposites (Ag—10, Ag—0.1, Ag—0.01) (A) and confocal Raman spectra of pure CS and bionanocomposites (Ag—10, Ag—0.1, Ag—0.01) (B).

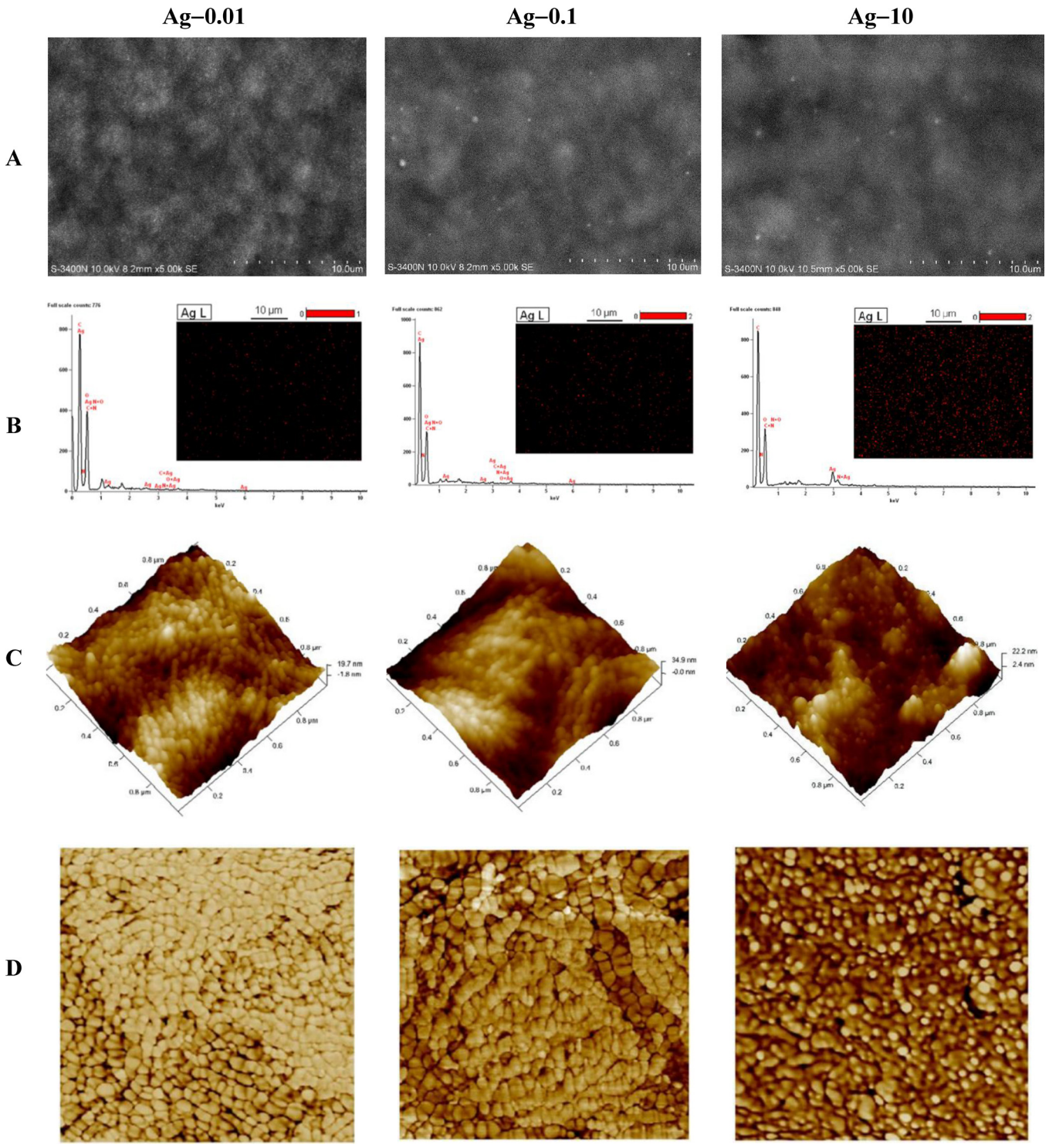

Fig. 6. Morphology of coatings with SEM (A), EDX of AgNPs embedded CS bionanocomposites (B), topographical analysis with AFM as height image (C) and phage profile on scale 0° to 50° (D) for Ag—0.01, Ag—0.1 and Ag—10. The scan width is 1000 nm for phase images.

3.6. Surface morphology and topography

3.6.1. Scanning electron microscopy (SEM/EDX) analysis

SEM micrographs (Fig. 6A) and EDX spectra (Fig. 6B) of the bionanocomposite coatings revealed smooth surfaces with micrometer size aggregates and uniformly distributed AgNPs onto Ti substrates. Apparently the aggregates tend to be larger for Ag—0.01 and smaller and better dispersed in the case of Ag—10. The EDX analysis detected C, N, and O attributed to the polymer matrix, and Ag from the embedded AgNPs. The elemental mappings inserted in EDX spectra reveal that AgNPs are uniformly distributed especially for the higher Ag concentrations (Ag—0.1 and Ag—10), supporting the hypothesis of partial agglomeration of AgNPs in Ag—0.01.

The compositional at% make-ups comprised <0.01 Ag (Ag—0.01), 0.04 Ag (Ag—0.1) and 0.47 Ag (Ag—10). The elemental mapping

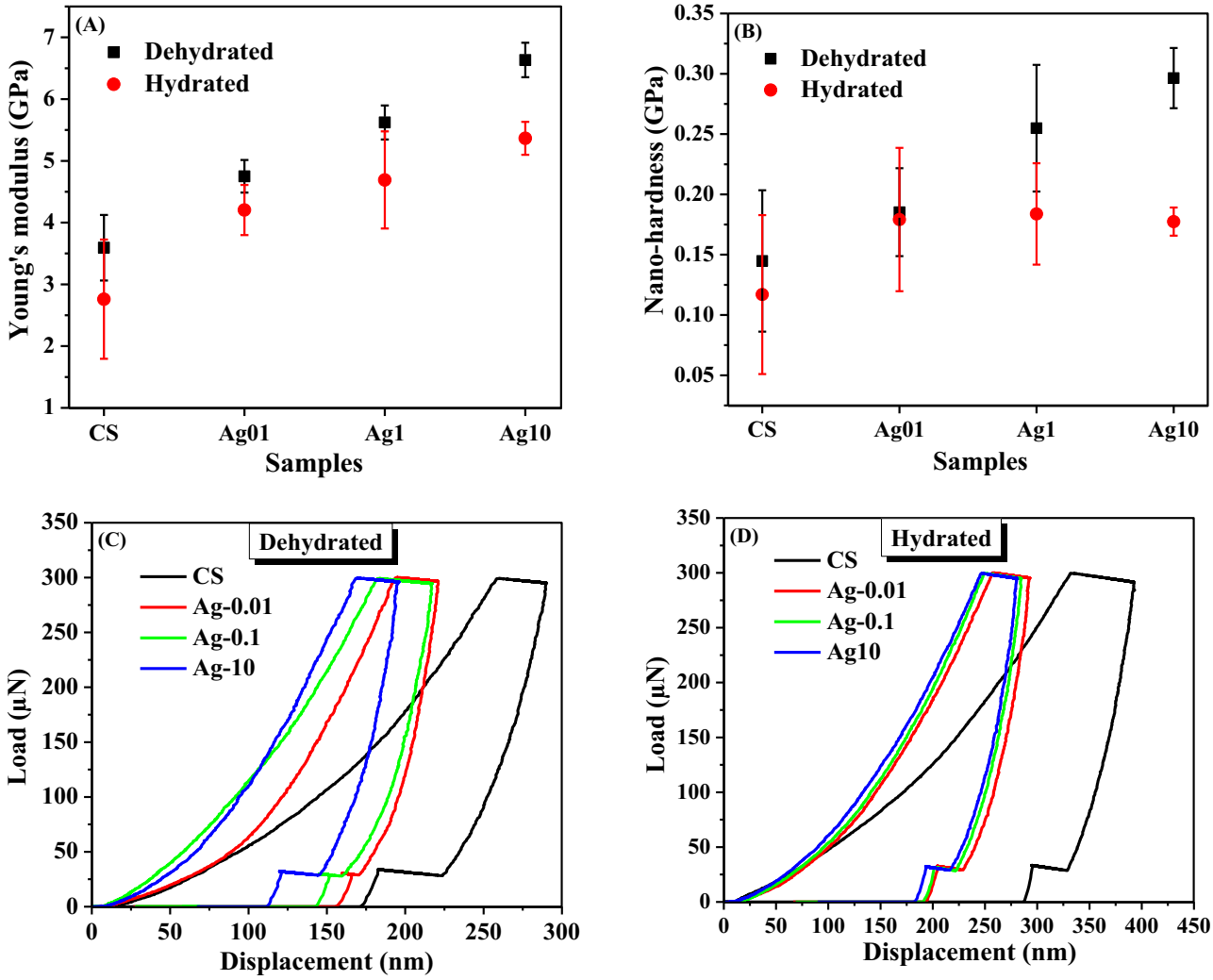

Fig. 7. Relative change in (A) Young's modulus (B) nanohardness of dehydrated and hydrated specimens and representative load-unload cycles of (C) dehydrated specimens (D) hydrated specimens. Error bars represent the standard deviations in 20 analyses.

and compositional analysis revealed that AgNPs were uniformly distributed through the coatings and an Ag at% ratio of ~10 for Ag—10 and Ag—0.1 samples, as expected.

3.6.2. *Atomic force microscopy analysis*

SEM analysis did not provide enough elucidation about the growth behavior of the coatings and how the polymeric coverage of AgNPs would likely influence antimicrobial activity. Therefore, tapping mode AFM was also used to assess complementary features of coating surfaces. Height (Fig. 6C) and phase contrast (Fig. 6D) AFM images of bionanocomposite coatings were analyzed to assess the surface topography features. Phase contrast structure analysis revealed that the surfaces of all samples were homogenously covered with nanosized granulated structures possibly formed by an intricacy of CS with PVA-capped AgNPs. The Ag—0.01 and Ag—0.1 surfaces exhibited smaller and more uniform granular structures in comparison with Ag—10. The average sizes of these granules were estimated as 42 ± 26 nm ($n \approx 130$), 38 ± 18 nm ($n \approx 170$) and 32 ± 13 nm ($n \approx 200$), for Ag—0.01, Ag—0.1 and Ag—10, respectively. The 3D surface images reveal micron sized clusters with evenly distributed nanosized granules. These images corroborate the surface morphological features observed by SEM.

These images illustrate the coatings are formed by nanometer sized granulated islands uniformly distributed throughout the surfaces. The surface roughness values of these bionanocomposite coatings were recorded as 10 ± 5 nm, 16 ± 6 nm and 19 ± 4 nm for Ag—10, Ag—0.1 and Ag—0.01, respectively, depicting their high smoothness features. The phase contrasts consistently observed across the scanned regions depended more on composition and local mechanical differences than on surface topography of the coatings (McLean & Sauer, 1997). This observation indicates that CS-AgNPs aggregates consist of a crystalline AgNPs cores and surrounding amorphous CS capsules.

3.7. *Particle size analyses*

To assess the real dimensions of AgNPs, three different methods (XRD, DLS and AFM) were attempted. Using the Scherrer formula, the crystallite diameters calculated over the (1 1 1) reflection were 26 nm, 25 nm and 16 nm for Ag—0.01, Ag—0.1 and Ag—10, respectively. This approach does not account for eventual agglomeration of primary particles. DLS instead gives more accurate information about the distribution of hydrodynamic sizes of nanoparticles irrespective of being mono- or poly-crystalline, provided that they are well dispersed. Therefore, special care was taken in sufficiently diluting and sonicating (10 min) the AgNPs sols for DLS analysis. The resulting mean sizes were 45 nm, 30 nm and 24 nm for Ag—0.01, Ag—0.1 and Ag—10, respectively. For all samples,

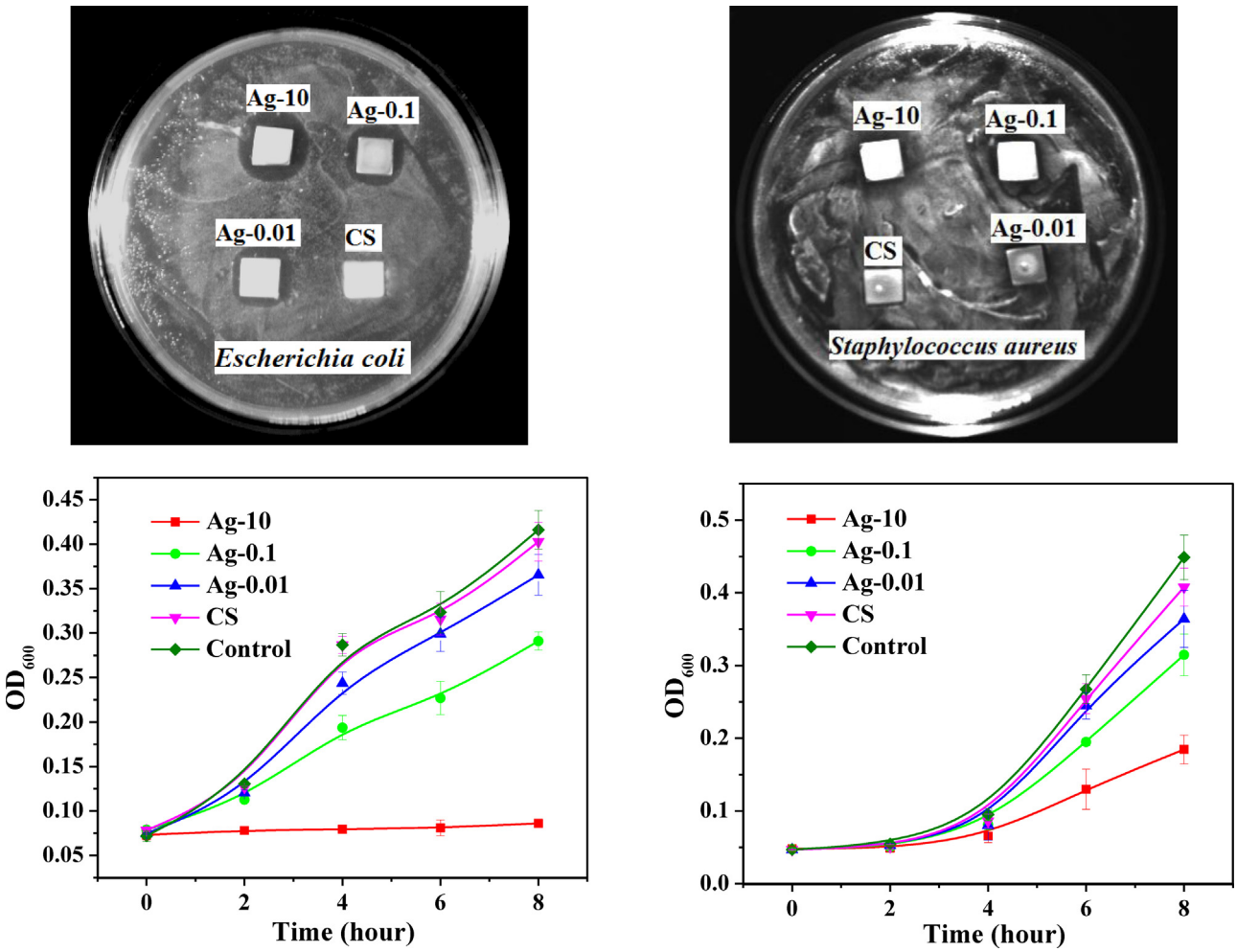

Fig. 8. Inhibition zone (above) and growth curve (below) of *E. coli* and *S. aureus* in TGY broth against different bionanocomposite coated specimens. Error bars represent standard deviations of triplicate experiments.

polydispersity indexes (PDI) were smaller than 0.35, a clear indication about the monodispersity of AgNPs in the sols. The larger sizes determined by DLS in comparison to XRD can be understood considering that hydrodynamic diameter accounts for the real diameter of a nanoparticle plus 2 fold the thickness of the adsorbed layer, including the electrical double layer to keep the particles away from each other. The AFM images of AgNPs embedded in the coatings suggest they were spherical in shape, appearing as single nanoparticles, clusters and aggregates randomly distributed over the Ti substrate.

3.8. Mechanical evaluation of the coatings

The elastic modulus and hardness of bionanocomposite coatings on Ti substrates were determined under both dry and hydrated conditions using the classical Oliver–Pharr method (Oliver & Pharr, 1992). The load displacement curves and the measured mechanical properties are plotted in Fig. 7. It can be seen that the embedded AgNPs reinforced the polymer matrix and enhanced the mechanical stability of coatings, benefits that increased with increasing nanofiller contents. With the addition of AgNPs, the elastic modulus of bionanocomposites under dry conditions gradually increased from 3.6 ± 0.5 GPa for unreinforced CS coating to 4.8 ± 0.3 GPa (Ag—0.01), 5.6 ± 0.3 GPa (Ag—0.1) and 6.6 ± 0.3 GPa (Ag—10). This last value is almost twice that of pure CS coating and besides the presence of AgNPs, the dipolar chain interactions between amine groups of CS and OH groups of PVA are also likely to contribute to the observed enhancements in mechanical properties of the coatings.

Relatively to dry samples, the elastic moduli of the coatings under hydrated conditions decreased by 23%, 11%, 16% and 19% for CS, Ag—0.01, Ag—0.1 and Ag—10, respectively. The loss in stiffness of coatings upon hydration becomes gradually more obvious with increasing contents of AgNPs. In any case, the elastic moduli of hydrated coatings are significantly higher than the values reported for CS based materials.

Similar variation trends discussed for elastic moduli as a function of AgNPs content were determined for nanohardness under dry and hydrated conditions. The smoothness of nanoindentation curves reflects the good homogeneity of coatings. The plausible formation of a dense network of intercalated CS and PVA chains mitigates water degradation of the composite coating, thereby justifying the plasticization effect of PVA. These results highlight the potential benefits of reinforcing polymeric implant coatings with nanofillers and preventing structural integrity losses of natural polymers like CS.

3.9. Silver ion release and antibacterial tests

The silver ion release profiles from bionanocomposite coatings along a time period of 2 h are shown in Fig. S2 (Supporting information S2). An apparent plateau was reached for Ag—0.01 after about

20 h, while a sustainable slow release up to ~100 h was observed from the Ag—0.1 coating. The faster but more sustainable release of Ag^+ was presented by Ag—10 coating, which after 120 h did not show any trend toward a plateau.

Suitable Ag^+ release profiles are the key to grant the antibacterial action of the coatings in the early stage of implantation when the chance of bacterial infection is more. The bactericidal results obtained by the modified disc diffusion and growth inhibition studies are shown in Fig. 8. The method aimed at assessing the antibacterial activity of bionanocomposite coatings at and near the surface. The second one was employed to analyze the antibacterial activity of coating against the bacterial infection of body fluid around the implant, mimicking closely the situation in clinical application. CS exhibited no bactericidal activity as no inhibition zone could be observed in modified disc diffusion test. This could be attributed to the non-protonated state of CS after neutralization in NaOH. Similarly, almost no inhibition against the growth of *E. coli* and *S. aureus* could be detected for CS coating that behaved like the control, indicating that CS coatings were ineffective in preventing bacterial growth around the implant area. The antibacterial activity of bionanocomposites revealed to be directly related to the concentration of AgNPs, with Ag—10 showing the largest inhibition zone in diffusion assay and the lowest OD_{600} at all predetermined time intervals in growth inhibition curves. The growth of *E. coli* was almost completely inhibited as observed by the next to nothing increase in OD_{600} for Ag—10. Relatively to *S. aureus*, no differences in the OD_{600} could be detected along the first 2 h, because in this assay dead cells are also considered in optical reading. After incubation for 2 h, there were significant differences in OD_{600} between the bionanocomposite coatings and the control, and after 4 h the growth inhibition curve reveals the bactericidal activity. The bactericidal action of AgNPs might be exerted through different mechanisms. The main mechanism derives from the ability of AgNP/Ag^+ to induce oxidative stress by reactive oxygen species (ROS) (Choi & Hu, 2008; Kittler et al., 2010). Another possible mechanism for antimicrobial action is the electrostatic interactions between AgNPs/Ag^+ and bacterial cell membranes molecules, which could result in depolarization of membrane followed by bacteria death (Choi & Hu, 2008; Mahmoudi & Serpooshan, 2012). These results enable concluding that CS coatings embedding AgNPs can inhibit infection from and G^+ bacteria without using antibiotics. But the efficacy of the bionanocomposite coatings is higher toward G^- bacteria.

4. Conclusions

Monodispersed and crystalline PVA-capped AgNPs could be synthesized through a clean and facile microwave approach. This polyol reduction method neither involves any harmful chemicals nor produces any by-product, therefore offering attractive features for the synthesis of metal nanoparticles for medical applications. Under the constant concentration of PVA used, particle sizes increased with decrease silver content. AFM analysis of the bionanocomposite surface coatings on Ti substrates revealed globular patterns of AgNPs encapsulated in the polymer matrix. Such a structure assured a sustainable long term release of Ag^+ ions that confer to the coatings an effective antibacterial activity. The mechanical stability of the bionanocomposite coatings was enhanced in comparison to the fragile nature of CS by the blending, plasticizing and reinforcing effects of PVA-capped AgNPs and the benefits increased with increasing inorganic contents. Accordingly, the mechanical properties of the bionanocomposite coatings even under hydrated conditions were better than those of pure CS coatings measured under dry conditions. The roughness values measured for the coatings revealed very smooth surfaces. Detailed studies about cytocompatibility of the coatings and how their mechanical strength influence cell viability, cell attachment, and their proliferation rate are currently under investigation and will be reported in future.

Acknowledgements

The financial assistance received from Department of Science and Technology, Ministry of Science and Technology, DST (Reference: SB/FT/CS-101/2012(SR)), India is acknowledged. The facilities availed from Central Instrumentation Facility, Department of Physics and Interdisciplinary Program for Life Sciences (IPLS) of Pondicherry University are acknowledged. The support from CICECO, University of Aveiro, Portugal is also acknowledged.

Appendix A. Supplementary data

Supplementary data associated with this article can be found, in the online version, at http://dx.doi.org/10.1016/j.carbpol.2014.12.027.

References

Adden, N., Gamble, L. J., Castner, D. G., Hoffmann, A., Gross, G., & Menzel, H. (2006). Synthesis and characterization of biocompatible polymer interlayers on titanium implant materials. *Biomacromolecules*, *7*, 2552–2559.

Angadi, S. C., Manjeshwar, L. S., & Aminabhavi, T. M. (2011). Stearic-acid coated chitosan-based interpenetrating polymer network microspheres: Controlled release characteristics. *Industrial and Engineering Chemistry Research*, *50*, 4504–4514.

Bo, L., Yang, W., Chen, M., Gao, J., & Xue, Q. (2009). A simple and 'green' synthesis of polymer-based silver colloids and their antibacterial properties. *Chemistry and Biodiversity*, *6*, 111–116.

Bohren, C. F., & Huffman, D. R. (1983). *Absorption and scattering of light by small particles*. New York, NY: Wiley.

Choi, O., & Hu, Z. (2008). Size dependent and reactive oxygen species related nanosilver toxicity to nitrifying bacteria. *Environmental Science and Technology*, *42*, 4583–4588.

Chuang, W.-Y., Young, T.-H., Yao, C.-H., & Chiu, W.-Y. (1999). Properties of the poly(vinyl alcohol)/chitosan blend and its effect on the culture of fibroblast in vitro. *Biomaterials*, *20*, 1479–1487.

Du, W.-L., Niu, S.-S., Xu, Y.-L., Xu, Z.-R., & Fan, C.-L. (2009). Antibacterial activity of chitosan tripolyphosphate nanoparticles loaded with various metal ions. *Carbohydrate Polymers*, *75*, 385–389.

Gao, J., Fu, J., Lin, C., Lin, J., Han, Y., Yu, X., et al. (2004). Formation and photoluminescence of silver nanoparticles stabilized by a two-armed polymer with a crown ether core. *Langmuir*, *20*, 9775–9779.

Gelder, J. D., Gussem, K. D., Vandenabeele, P., & Moens, L. (2007). Reference database of Raman spectra of biological molecules. *Journal of Raman Spectroscopy*, *38*, 1133–1147.

Hebbalalu, D., Lalley, J., Nadagouda, M. N., & Varma, R. S. (2013). Greener techniques for the synthesis of silver nanoparticles using plant extracts, enzymes, bacteria, biodegradable polymers, and microwaves. *ACS Sustainable Chemistry and Engineering*, *1*, 703–712.

Hu, B., Wang, S.-B., Wang, K., Zhang, M., & Yu, S.-H. (2008). Microwave-assisted rapid facile green synthesis of uniform silver nanoparticles: Self-assembly into multilayered films and their optical properties. *Journal of Physical Chemistry C*, *112*, 11169–11174.

Jiao, H., Yao, J., Yang, Y., Chen, X., Lin, W., Li, Y., et al. (2009). Chitosan/polyglycolic acid nerve grafts for axon regeneration from prolonged axotomized neurons to chronically denervated segments. *Biomaterials*, *30*, 5004–5018.

Jin, L., & Bai, R. (2002). Mechanisms of lead adsorption on chitosan/PVA hydrogel beads. *Langmuir*, *18*, 9765–9770.

Kahrilas, G. A., Haggren, W., Read, R. L., Wally, L. M., Fredrick, S. J., Hiskey, M., et al. (2014). Investigation of antibacterial activity by silver nanoparticles prepared by microwave-assisted green syntheses with soluble starch, dextrose, and arabinose. *ACS Sustainable Chemistry and Engineering*, *2*, 590–598.

Kahrilas, G. A., Wally, L. M., Fredrick, S. J., Hiskey, M., Prieto, A. L., & Owens, J. E. (2014). Microwave-assisted green synthesis of silver nanoparticles using orange peel extract. *ACS Sustainable Chemistry and Engineering*, *2*, 367–376.

Kim, I.-Y., Seo, S.-J., Moon, H.-S., Yoo, M.-K., Park, I.-Y., Kim, B.-C., et al. (2008). Chitosan and its derivatives for tissue engineering applications. *Biotechnology Advances*, *26*, 1–21.

Kittler, S., Greulich, C., Diendorf, J., Koller, M., & Epple, M. (2010). Toxicity of silver nanoparticles increases during storage because of slow dissolution under release of silver ions. *Chemistry of Materials*, *22*, 4548–4554.

Kreibig, U., & Vollmer, M. (1995). *Optical properties of metal clusters*. New York, NY: Springer-Verlag.

Kubo, S., & Kadla, J. F. (2003). The formation of strong intermolecular interactions in immiscible blends of poly(vinyl alcohol) (PVA) and lignin. *Biomacromolecules*, *4*, 561–567.

Kuo, Y.-C., & Ku, I.-N. (2008). Cartilage regeneration by novel polyethylene oxide/chitin/chitosan scaffolds. *Biomacromolecules*, *9*, 2662–2669.

Lansdown, A. B. G. (2002). Silver I: Its antibacterial properties and mechanism of action. *Journal of Wound Care*, *11*, 125–130.

Lara, H. H., Ayala-Nunez, N. V., Turrent, L. d. C. I., & Padilla, C. R. (2010). Bactericidal effect of silver nanoparticles against multidrug-resistant bacteria. *World Journal of Microbiology and Biotechnology*, *26*, 615–621.

Liang, C., Wang, H., Yang, J., Cai, Y., Hu, X., Yang, Y., et al. (2013). Femtosecond laser-induced micropattern and Ca/P deposition on Ti implant surface and its acceleration on early osseointegration. *ACS Applied Material and Interfaces*, *5*, 8179–8186.

Lillo, L. E., & Matsuhiro, B. (1997). Chemical modifications of carboxylated chitosan. *Carbohydrate Polymers*, *34*, 397–401.

Lina, H.-Y., & Chen, J.-H. (2013). Osteoblast differentiation and phenotype expressions on chitosan-coated Ti-6Al-4V. *Carbohydrate Polymers*, *97*, 618–626.

Liu, J., Sonshine, D. A., Shervani, S., & Hurt, R. H. (2010). Controlled release of biologically active silver from nanosilver surfaces. *ACS Nano*, *4*, 6903–6913.

Magiorakos, A.-P., Srinivasan, A., Carey, R. B., Carmeli, Y., Falagas, M. E., Giske, C. G., et al. (2012). Multidrug-resistant, extensively drug-resistant and pandrug-resistant bacteria: an international expert proposal for interim standard definitions for acquired resistance. *European Society of Clinical Microbiology and Infectious Diseases*, *18*, 268–281.

Mahmoudi, M., & Serpooshan, V. (2012). Silver-coated engineered magnetic nanoparticles are promising for the success in the fight against antibacterial resistance threat. *ACS Nano*, *6*, 2656–2664.

Maity, D., Bain, M. K., Bhowmick, B., Sarkar, J., Saha, S., Acharya, K., et al. (2011). In situ synthesis, characterization, and antimicrobial activity of silver nanoparticles using water soluble polymer. *Journal of Applied Polymer Science*, *122*, 2189–2196.

Malafaya, P. B., & Reis, R. L. (2009). Bilayered chitosan-based scaffolds for osteochondral tissue engineering: Influence of hydroxyapatite on in vitro cytotoxicity and dynamic bioactivity studies in a specific double-chamber bioreactor. *Acta Biomaterialia*, (5), 644–660.

Mansur, H. S., Costa, E. d. S., Mansur, A. A. P., & Barbosa-Stancioli, E. F. (2009). Cytocompatibility evaluation in cell-culture systems of chemically crosslinked chitosan/PVA hydrogels. *Materials Science and Engineering: C*, *29*, 1574–1583.

Matsumura, S., Tomizawa, N., Toki, A., Nishikawa, K., & Toshima, K. (1999). Novel poly(vinyl alcohol)-degrading enzyme and the degradation mechanism. *Macromolecules*, *32*, 7753–7761.

McLean, R. S., & Sauer, B. B. (1997). Tapping-mode AFM studies using phase detection for resolution of nanophases in segmented polyurethanes and other block copolymers. *Macromolecules*, *30*, 8314–8317.

Mi, F.-L., Wu, Y.-B., Shyu, S.-S., Schoung, J.-Y., Huang, Y.-B., Tsai, Y.-H., et al. (2002). Control of wound infections using a bilayer chitosan wound dressing with sustainable antibiotic delivery. *Journal of Biomedical Materials Research*, *59*, 438–449.

Mironenko, A., Modin, E., Sergeev, A., Voznesenskiy, S., & Bratskaya, S. (2014). Fabrication and optical properties of chitosan/Ag nanoparticles thin film composites. *Chemical Engineering Journal*, *244*, 457–463.

Nadagouda, M. N., Speth, T. F., & Varma, R. S. (2011). Microwave-assisted green synthesis of silver nanostructures. *Accounts of Chemical Research*, *44*, 469–478.

Nishio, Y., Haratani, T., Takahashi, T., & Manley, R. S. J. (1989). Cellulose/poly(vinyl alcohol) blends: An estimation of thermodynamic polymer-polymer interaction by melting-point-depression analysis. *Macromolecules*, *22*, 2547–2549.

Oliver, W. C., & Pharr, G. M. (1992). Improved technique for determining hardness and elastic modulus using load and displacement sensing indentation experiments. *Journal of Materials Research*, *7*, 1564–1583.

Podsiadlo, P., Paternel, S., Rouillard, J.-M., Zhang, Z., Lee, J., Lee, J.-W., et al. (2005). Layer-by-layer assembly of nacre-like nanostructured composites with antimicrobial properties. *Langmuir*, *21*, 11915–11921.

Porel, S., Singh, S., Harsha, S. S., Rao, D. N., & Radhakrishnan, T. P. (2005). Nanoparticle-embedded polymer: In situ synthesis, free-standing films with highly monodisperse silver nanoparticles and optical limiting. *Chemistry of Materials*, *17*, 9–12.

Rai, M., Yadav, A., & Gade, A. (2009). Silver nanoparticles as a new generation of antimicrobials. *Biotechnology Advances*, *27*, 76–83.

Ratner, B. D., Hoffman, A. S., Schoen, F. J., & Lemons, J. E. (1996). *Biomaterial science—An introduction to materials in medicine*. U.S.A.: Academic Press.

Roldan, M. V., Scaffardi, L. B., Sanctis, O. d., & Pellegri, N. (2008). Optical properties and extinction spectroscopy to characterize the synthesis of amine capped silver nanoparticles. *Materials Chemistry and Physics*, *112*, 984–990.

She, C. Y., Dinh, N. D., & Tu, A. T. (1974). Laser raman scattering of glucosamine, *N*-acetylglucosamine, and glucuronic acid. *Biochimica et Biophysica Acta*, *372*, 345–357.

Simo, A., Polte, J., Pfander, N., Vainio, U., Emmerling, F., & Rademann, K. (2012). Formation mechanism of silver nanoparticles stabilized in glassy matrices. *Journal of the American Chemical Society*, *134*, 18824–18833.

Smitha, S. L., Nissamudeen, K. M., Philip, Daizy, & Gopchandran, K. G. (2008). Studies on surface plasmon resonance and photoluminescence of silver nanoparticles. *Spectrochimica Acta, A*, *71*, 186–190.

Taglietti, A., Fernandez, Y. A. D., Amato, E., Cucca, L., Dacarro, G., Grisoli, P., et al. (2012). Antibacterial activity of glutathione-coated silver nanoparticles against gram positive and gram negative bacteria. *Langmuir*, *28*, 8140–8148.

Tiwari, A. D., Mishra, A. K., Mishra, S. B., Kuvarega, A. T., & Mamba, B. B. (2013). Stabilisation of silver and copper nanoparticles in a chemically modified chitosan matrix. *Carbohydrate Polymers*, *92*, 1402–1407.

Vigneshwaran, N., Nachane, R. P., Balasubramanya, R. H., & Varadarajan, P. V. (2006). A novel one-pot 'green' synthesis of stable silver nanoparticles using soluble starch. *Carbohydrate Research*, *341*, 2012–2018.

Wan, Y., Wu, H., Yu, A., & Wen, D. (2006). Biodegradable polylactide/chitosan blend membranes. *Biomacromolecules*, *7*, 1362–1372.

Wang, X., Du, Y., Fan, L., Liu, H., & Hu, Y. (2005). Chitosan–metal complexes as antimicrobial agent: Synthesis, characterization and structure-activity study. *Polymer Bulletin*, *55*, 105–113.

Wei, D., Sun, W., Qian, W., Ye, Y., & Ma, X. (2009). The synthesis of chitosan-based silver nanoparticles and their antibacterial activity. *Carbohydrate Research*, *344*, 2375–2382.

Williams, R. L., Doherty, P. J., Vince, D. G., Grashoff, G. J., & Williams, D. F. (1989). The biocompatibility of silver. *Critical Review in Biocompatibility*, *5*, 221–243.

Xing, Z.-C., Chae, W.-P., Baek, J.-Y., Choi, M.-J., Jung, Y., & Kang, I.-K. (2010). In vitro assessment of antibacterial activity and cytocompatibility of silver-containing PHBV nanofibrous scaffolds for tissue engineering. *Biomacromolecules*, *11*, 1248–1253.

Zhang, K., Peschel, D., Helm, J., Groth, T., & Fischer, S. (2011). FT Raman investigation of novel chitosan sulfates exhibiting osteogenic capacity. *Carbohydrate Polymers*, *83*, 60–65.

Zhou, Y., Yang, D., Chen, X., Xu, Q., Lu, F., & Nie, J. (2008). Electrospun water-soluble carboxyethyl chitosan/poly(vinyl alcohol) nanofibrous membrane as potential wound dressing for skin regeneration. *Biomacromolecules*, *9*, 349–354.